

Plug-and-play Shape Refinement Framework for Multi-site and Lifespan Brain Skull Stripping

Yunxiang Li^{1,2}, Ruilong Dan², Shuai Wang³, Yifan Cao², Xiangde Luo⁴,
Chenghao Tan², Gangyong Jia², Huiyu Zhou⁵, You Zhang¹, Yaqi Wang^{2,6}✉,
Li Wang⁷✉

¹ Department of Radiation Oncology, University of Texas Southwestern Medical Center, Dallas, USA

² Hangzhou Dianzi University, Hangzhou, China

³ School of Mechanical, Electrical and Information Engineering, Shandong University, Weihai, China

⁴ University of Electronic Science and Technology of China, Chengdu, China

⁵ School of Computing and Mathematical Sciences, University of Leicester, UK

⁶ Communication University of Zhejiang, Hangzhou, China

wangyaqi@cuz.edu.cn

⁷ Developing Brain Computing Lab, Department of Radiology and BRIC, University of North Carolina at Chapel Hill, Chapel Hill, USA

li_wang@med.unc.edu

Abstract. Skull stripping is a crucial prerequisite step in the analysis of brain magnetic resonance images (MRI). Although many excellent works or tools have been proposed, they suffer from low generalization capability. For instance, the model trained on a dataset with specific imaging parameters cannot be well applied to other datasets with different imaging parameters. Especially, for the lifespan datasets, the model trained on an adult dataset is not applicable to an infant dataset due to the large domain difference. To address this issue, numerous methods have been proposed, where domain adaptation based on feature alignment is the most common. Unfortunately, this method has some inherent shortcomings, which need to be retrained for each new domain and requires concurrent access to the input images of both domains. In this paper, we design a plug-and-play shape refinement (PSR) framework for multi-site and lifespan skull stripping. To deal with the domain shift between multi-site lifespan datasets, we take advantage of the brain shape prior, which is invariant to imaging parameters and ages. Experiments demonstrate that our framework can outperform the state-of-the-art methods on multi-site lifespan datasets.

Keywords: Skull stripping · Transformer · Domain adaptation · Shape dictionary · Lifespan brain

Y. Li and R. Dan—Equal contribution.

1 Introduction

Skull stripping, the separation of brain tissue from non-brain tissue, is a critical preprocessing step for the characterization of brain MRI. Plenty of skull stripping tools have been proposed, e.g., morphology-based method: Brain Surface Extractor (BSE) [1] and surface-based method: Brain Extraction Tool (BET) [2]. Compared with traditional skull stripping tools, deep learning has recently been proven more suitable for skull stripping, where 3D U-Net is the most popular backbone [3,4]. Based on it, 3D Residual U-Net, 3D Attention UNet, and TransBTS are proposed to get better segmentation performance [5,6,7]. In addition, some specific methods have been designed, e.g., Zhong et al. proposed a domain-invariant knowledge-guided attention network for brain skull stripping [8]. Zhang et al. proposed a flattened residual network for infant MRI skull stripping [9]. However, the high performance of deep learning-based methods requires that the training and testing datasets share a similar data distribution, which is hardly met due to a variety of device manufacturers, magnetic field strength, and acquisition protocols. Moreover, there is also a substantial data distribution difference across lifespan, e.g., the adult and infant brain MRI in Fig. 1, where the infant’s brain is undergoing myelination and maturation.

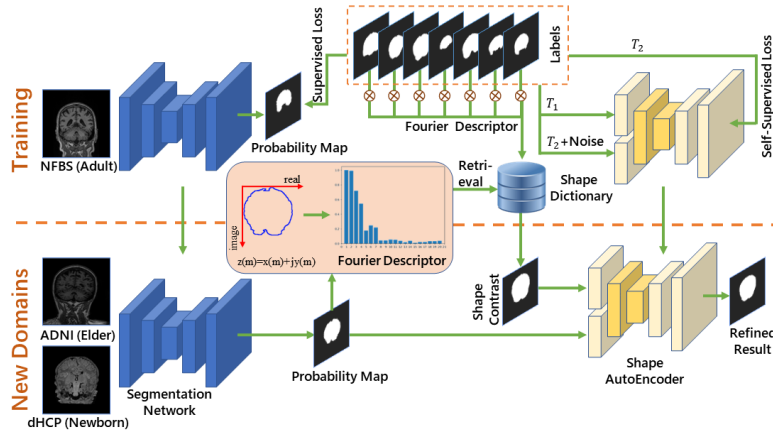


Fig. 1. A schematic overview of our proposed plug-and-play shape refinement framework.

Many efforts have been devoted to addressing the domain shift problem. Among them, the most widely used method is domain adaptation to align the latent feature distributions of the two domains [10,11]. Unfortunately, there are some inherent limitations, including the need for retraining for each new domain and concurrent access to the input images of both domains. It is well known that medical images are difficult to share due to privacy. Compared with the original image, manual labels contain much less privacy information and are

easier to share. Therefore, we propose a plug-and-play shape refinement (PSR) framework in this work. The main contributions of our method are three-fold: **1)** A novel plug-and-play segmentation result refinement framework is designed. **2)** A shape dictionary based on the Fourier Descriptors [12] is proposed to fully utilize the anatomical prior knowledge of the brain shape. **3)** To better model the overall shape information, we designed a shape AutoEncoder (SAE) based on Shuffle Transformer.

2 Method

2.1 Overall Architecture

The overall framework of PSR is illustrated in Fig. 1. Specifically, we can arbitrarily take a model trained in the source domain as the segmentation network. Fourier Descriptors [12] of the source labels are computed to build a shape dictionary. Then, the new domain image is directly input into the model, and Fourier Descriptors of the segmentation results are computed. Through it, we can retrieve a label with the closest shape from the shape dictionary. Finally, the segmentation results, together with the retrieved labels, serve as inputs into SAE to further refine the segmentation results.

2.2 Shape Dictionary

To make full use of the anatomy prior knowledge of brain shape, we calculate the corresponding Fourier Descriptors for each subject according to the source labels and store them in the dictionary. Assuming source labels $L^s = \{l_i^s\}_{i=1}^{|L^s|}$, the constructing process of shape dictionary D^s is defined as Eq. (1)

$$D^s = \{d_i^s \mid d_i^s = F(l_i^s)\}_{i=1}^{|L^s|} \quad (1)$$

where F is the Fourier Descriptor for a quantitative representation of closed shapes independent of their starting point, scale, location, and rotation. The whole process of computing Fourier Descriptors consists of three steps: (1) Establish a coordinate system in the upper left corner of the boundary, and the coordinate axis is tangent to the boundary. (2) Take the two axes as real and imaginary numbers respectively, and the coordinates of points (x_m, y_m) on the boundary are expressed in complex numbers $z(m) = x_m + jy_m$. (3) The discrete Fourier transform (DFT) is applied to the above coordinates to obtain the Fourier Descriptor of the boundary shape, which is defined as $Z(k)$ in Eq. (2).

$$Z(k) = \frac{1}{N} \sum_{m=0}^{N-1} z(m)e^{-j2\pi mk/N}, k = 0, 1, 2, \dots, N-1 \quad (2)$$

where N is the amount of the boundary points. Specifically, we choose 10 low-frequency coefficients as the final Fourier Descriptors, which is sufficient to achieve the required accuracy for retrieving [13].

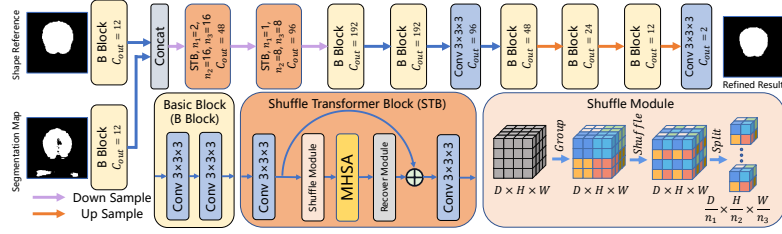


Fig. 2. A schematic overview of our Shape AutoEncoder. The skip connection of the U-shaped structure is not shown for simplicity.

2.3 Shape AutoEncoder (SAE)

The Shape AutoEncoder is designed to further refine the segmentation results based on both segmentation maps from the segmentation network and the shape reference from the shape dictionary, with the detailed structure shown in Fig. 2. To better extract global information such as overall shape, Transformer-based methods are good candidates [14,15,16]. Based on 2D Shuffle Transformer [17], we design a 3D Shuffle Transformer to capture global capability.

Shuffle Transformer: Our shuffle Transformer mixes the voxel features regularly, then evenly divides them into non-overlapping groups. Specifically, Shuffle Module takes the feature X as input and outputs shuffled blocks X^b ; thus it can be formulated through Eq. (3).

$$X^b = \{x_i^b \mid x_i^b = \text{Split}(\text{Shuffle}(\text{Group}(X, i))), x_i^b \in \mathbb{R}^{\frac{D}{n_1} \times \frac{H}{n_2} \times \frac{W}{n_3}}\}_{i=1}^{(n_1 \times n_2 \times n_3)} \quad (3)$$

where the details of Group, Shuffle, and Split are depicted in Fig. 2. After these operations we obtain a total number of $(n_1 \times n_2 \times n_3)$ shuffled blocks x^b , each with a size of $\frac{D}{n_1} \times \frac{H}{n_2} \times \frac{W}{n_3}$. Subsequently, each group is computed by multi-head self-attention. Since our shuffle operation keeps the relative position of each element in the shuffled blocks as the same as the original feature block, our position encoding method is based on relative-distance-aware position encoding [18,19]. The query-key-value (QKV) attention [20] in each small block x^b can be computed by Eq. (4).

$$\text{Attention}(Q, K, V) = \text{softmax}\left(\frac{QK^T}{\sqrt{d_k}} + B\right)V \quad (4)$$

where Q , K , and V stand the query, key, and value matrices of dimension d_k respectively, and B denotes the position biases matrix.

Self-supervised Training of Shape AutoEncoder: As for the training process of SAE, it is based on self-supervision, meaning the supervisory signals are

generated by the input, and we use the shared source labels as the training images of SAE. Each image is processed by two kinds of random spatial transformations (T_1 and T_2). Specifically, our random spatial transformations contain random scaling, random rotation, and random clipping. Assume we have images $Y = \{y_i\}_{i=1}^\eta$ where η denotes the number of images, thus transformed images are generated via Eq. (5).

$$\begin{aligned} Y^{T_1} &= \{y_i^{T_1} \mid y_i^{T_1} = T_1(y_i)\}_{i=1}^\eta \\ Y^{T_2} &= \{y_i^{T_2} \mid y_i^{T_2} = T_2(y_i)\}_{i=1}^\eta \end{aligned} \quad (5)$$

To mimic the unreliable segmentation results caused by domain shift, random noises RN are added to T_2 through placing random false positive and false negative stain to generate $Y^{T_2 \circ RN}$ formulated by Eq. (6). The random noise is controlled by two variables: the amount and size of the noise. The hyperparameters of the random noise are discussed in the supplementary material.

$$Y^{T_2 \circ RN} = RN(Y^{T_2}) \quad (6)$$

Let $SAE(y_i^{T_1}, y_i^{T_2 \circ RN}; \theta)$ be the Shape AutoEncoder, thus refined outputs \hat{Y} are defined via Eq. (7).

$$\hat{Y} = SAE(Y^{T_1}, Y^{T_2 \circ RN}; \theta) \quad (7)$$

\hat{Y} and θ represent the prediction output and the trainable parameters of SAE respectively, and the self-supervised loss function of the SAE is defined by Eq. (8).

$$\begin{aligned} \mathcal{L}_{SAE}(\hat{Y}, Y^{T_2}) &= -\frac{1}{\eta} \sum_{i=1}^{\eta} (T_2(y_i) \times \ln(SAE(T_1(y_i), RN(T_2(y_i)); \theta)) \\ &\quad + (1 - T_2(y_i)) \times (1 - \ln(SAE(T_1(y_i), RN(T_2(y_i)); \theta)))) \end{aligned} \quad (8)$$

In this way, it can not only combine segmentation results and shape reference but also denoise and refine the unreliable segmentation results automatically through learning shape prior knowledge from the labels.

3 Implementation and Experiments

3.1 Datasets and Evaluation Metrics

We evaluated the proposed method on the publicly available dataset, where the source domain is from Neurofeedback Skull-stripped (NFBS) [21], and the new (target) domains are from Alzheimer’s Disease Neuroimaging Initiative (ADNI) [22] and Developing Human Connectome Project (dHCP) [23]. Note that subjects from NFBS are young adults from 21 to 45 years old and ADNI are older adults from 55 and 90 years old, and dHCP are newborns. After resampling and padding, the size of the individual scan is $256 \times 256 \times 256$ and each voxel size

is $1 \times 1 \times 1 \text{ mm}^3$. We selected 25 subjects from NFBS with manual labels as the training dataset and each 10 subjects from ADNI and dHCP as the testing dataset, and 3-fold cross-validation is used. It is worth noting that there is no available publicly manual label of dHCP, and thus we only compare the results by visual inspection. Due to the limited GPU memory, a sub-volume of size $64 \times 64 \times 64$ is used as the first stage segmentation network input. In order to better capture the overall shape, the input size of the Shape AutoEncoder is set to $8 \times 256 \times 256$, and the middle layer slice with the size of 256×256 is used to compute the Fourier Descriptors and retrieve the most similar shape from the dictionary. For all experiments described below, the Average Surface Distance (ASD), the Dice Coefficients (DICE), the sensitivity (SEN) and specificity (SPE) are chosen for evaluation metrics.

3.2 Implementation Details

All our experiments were based on the PyTorch framework and carried out on 4 Nvidia RTX 2080Ti GPUs. We trained our network from scratch for a total of 10000 iterators, and the parameters were updated by the Adam algorithm (momentum = 0.97, weight decay = 5×10^{-4}). We adopt a batch size of 4 and set the learning rate as 2×10^{-4} . Notedly, if there is no additional statement, our PSR is combined with 3D U-Net by default in this paper. The discussion of the hyperparameters is on the supplementary material.

Table 1. Comparison with the state-of-the-art methods on ADNI.

Method	ASD (mm)	DICE (%)	SPE (%)	SEN (%)
3D U-Net [3]	11.57±9.83	88.30±3.53	99.51±0.68	82.69±3.10
CycleGAN [24]	18.96±7.88	86.27±2.85	98.72±0.51	85.19±2.58
EMNet [25]	8.67±9.86	91.49±2.39	99.37±0.49	89.32±2.10
Tent [26]	7.19±6.24	90.52±1.70	99.64±0.28	85.60±2.18
PSR (3D U-Net)	4.63±0.98	91.57±1.38	99.55±0.15	88.09±2.67

3.3 Experimental Results on Cross-site Dataset

Our results are presented in Table. 1, and our method is combined with 3D U-Net, namely PSR (3D U-Net). We can observe that our method enhances the performance of 3D U-Net a lot. Moreover, our method outperforms the state-of-the-art domain adaptation method, i.e., EMNet. Interestingly, the ASD achieved by other methods was unexpectedly far higher than ours. This may be due to the fact that the training data from the source domain do not have the shoulder part, but the testing data in the new domain do have the shoulder, which is illustrated in Fig. 3. Our method is capable of identifying the segmentation result of the shoulder as unreliable results and excluding it from the brain tissues. We can also notice that the output of CycleGAN mistakenly identifies many non-brain

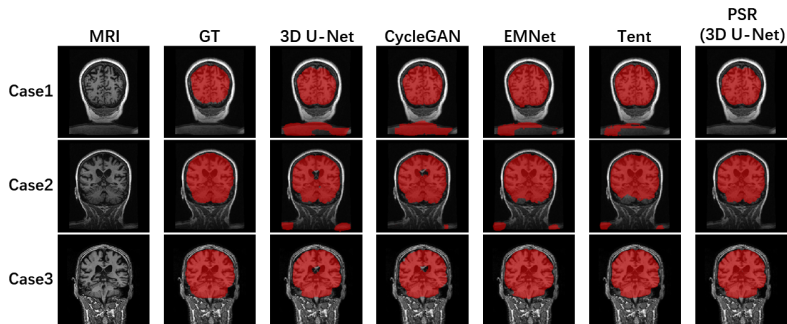


Fig. 3. Visualization of segmentation results on ADNI.

regions as the brain. Consequently, its performance is unexpectedly poorer than those obtained from the source model without domain adaptation.

In order to further test the potential of our PSR, we also combined it with other popular networks. As shown in Table. 2, the segmentation performances of all the networks have been enhanced a lot by combining with our PSR.

Table 2. Comparison with the state-of-the-art methods on ADNI.

Method	ASD (mm)	DICE (%)
3D Residual U-Net	13.73±9.69	88.99±4.19
PSR (3D Residual U-Net)	4.42±1.61	91.34±1.61
3D Attention U-Net	10.13±7.03	89.29±2.17
PSR (3D Attention U-Net)	4.06±0.76	91.22±0.99
TransBTS	12.31±12.26	88.80±4.67
PSR (TransBTS)	6.01±2.64	90.87±1.65
3D U-Net	11.57±9.83	88.30±3.53
PSR (3D U-Net)	4.63±0.98	91.57±1.38

3.4 Visualization Results on Newborns

We qualitatively compare the segmentation outputs of the proposed PSR and the 3D U-Net on the newborn. Although the infant shares a similar shape and basic structure with the adult, the infant’s brain develops rapidly throughout the first year of life, resulting in huge appearance differences from the adult. As shown in Fig. 4, 3D U-Net cannot achieve accurate brain tissues with fuzzy brain boundaries, while our method is able to generate smooth and reasonable segmentations.

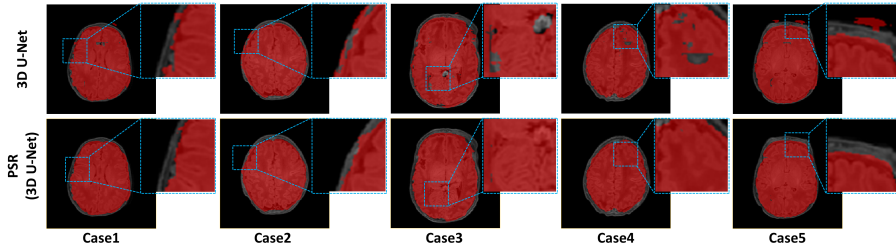


Fig. 4. Qualitative comparison of segmentation results on newborn brain MRI from dHCP.

3.5 Ablation Study

In order to verify the effectiveness of the main components of our proposed PSR, we conducted the following ablation study: a) implement our PSR without Shape AutoEncoder, referred to as PSR w/o SAE. b) implement our PSR without shape dictionary, that is, only the unrefined segmentation results are input to Shape AutoEncoder, referred to as PSR w/o SD. c) implement our PSR without shuffle Transformer, that is, replace the shuffle Transformer block with the basic convolution block, denoted as PSR w/o ST. Quantitative comparison results of the three variants along with the PSR are illustrated in Table 3. The proposed PSR achieves improved performance, especially in terms of important ASD and DICE metrics.

Table 3. Ablation study of our method.

Method	ASD (mm)	DICE (%)	SPE (%)	SEN (%)
PSR w/o SAE	11.57±9.83	88.30±3.53	99.51±0.68	82.69±3.10
PSR w/o SD	6.86±3.53	89.73±1.42	99.41±0.13	86.04±2.21
PSR w/o ST	6.39±4.24	90.62±1.40	99.76±0.13	84.79±2.66
PSR	4.63±0.98	91.57±1.38	99.55±0.15	88.09±2.67

4 Conclusion

In summary, we presented a plug-and-play shape refinement framework and successfully applied it to the skull stripping task on multi-site lifespan datasets. Our method consists of a shape dictionary and a Shape AutoEncoder. With the assistance of the shape dictionary, the Shape AutoEncoder makes full use of the anatomical prior knowledge to refine the unreliable segmentation results in the new domain. Experimental results demonstrated that the proposed method can enhance the performance of most networks and achieves better performance than the state-of-the-art unsupervised domain adaptation methods, and the proposed

Shape AutoEncoder can further enhance traditional skull stripping tools. Theoretically, our method can also be widely applied to other organ segmentation.

Acknowledgements. This work was supported in part by National Institutes of Health (Grant No. R01CA240808 and R01CA258987), National Natural Science Foundation of China (Grant No. U20A20386), Shandong Provincial Natural Science Foundation (Grant No. 2022HWYQ-041)

References

1. David W Shattuck, Stephanie R Sandor-Leahy, Kirt A Schaper, David A Rottenberg, and Richard M Leahy. Magnetic resonance image tissue classification using a partial volume model. *NeuroImage*, 13(5):856–876, 2001.
2. Stephen M Smith. Fast robust automated brain extraction. *Human brain mapping*, 17(3):143–155, 2002.
3. Özgün Çiçek, Ahmed Abdulkadir, Soeren S Lienkamp, Thomas Brox, and Olaf Ronneberger. 3d u-net: learning dense volumetric segmentation from sparse annotation. In *International conference on medical image computing and computer-assisted intervention*, pages 424–432. Springer, 2016.
4. Xiangde Luo, Wenjun Liao, Jieneng Chen, Tao Song, Yinan Chen, Shichuan Zhang, Nianyong Chen, Guotai Wang, and Shaoting Zhang. Efficient semi-supervised gross target volume of nasopharyngeal carcinoma segmentation via uncertainty rectified pyramid consistency. In *Medical Image Computing and Computer Assisted Intervention – MICCAI 2021*, pages 318–329, 2021.
5. Mobarakol Islam, VS Vibashan, V Jose, Navodini Wijethilake, Uppal Utkarsh, and Hongliang Ren. Brain tumor segmentation and survival prediction using 3d attention unet. In *International MICCAI Brainlesion Workshop*, pages 262–272. Springer, 2019.
6. Wei Yu, Bin Fang, Yongqing Liu, Mingqi Gao, Shenhai Zheng, and Yi Wang. Liver vessels segmentation based on 3d residual u-net. In *2019 IEEE International Conference on Image Processing (ICIP)*, pages 250–254. IEEE, 2019.
7. Wenxuan Wang, Chen Chen, Meng Ding, Hong Yu, Sen Zha, and Jiangyun Li. Transbts: Multimodal brain tumor segmentation using transformer. In *International Conference on Medical Image Computing and Computer-Assisted Intervention*, pages 109–119. Springer, 2021.
8. Tao Zhong, Fenqiang Zhao, Yuchen Pei, Zhenyuan Ning, Lufan Liao, Zhengwang Wu, Yuyu Niu, Li Wang, Dinggang Shen, Yu Zhang, et al. Dika-nets: Domain-invariant knowledge-guided attention networks for brain skull stripping of early developing macaques. *NeuroImage*, 227:117649, 2021.
9. Qian Zhang, Li Wang, Xiaopeng Zong, Weili Lin, Gang Li, and Dinggang Shen. Frnet: Flattened residual network for infant mri skull stripping. In *2019 IEEE 16th International Symposium on Biomedical Imaging (ISBI 2019)*, pages 999–1002. IEEE, 2019.
10. Yunxiang Li, Jingxiong Li, Ruilong Dan, Shuai Wang, Kai Jin, Guodong Zeng, Jun Wang, Xiangji Pan, Qianni Zhang, Huiyu Zhou, et al. Dispensed transformer network for unsupervised domain adaptation. *arXiv preprint arXiv:2110.14944*, 2021.
11. Qi Dou, Cheng Ouyang, Cheng Chen, Hao Chen, Ben Glocker, Xiahai Zhuang, and Pheng-Ann Heng. Pnp-adanet: Plug-and-play adversarial domain adaptation

- network at unpaired cross-modality cardiac segmentation. *IEEE Access*, 7:99065–99076, 2019.
12. Mark S. Nixon and Alberto S. Aguado. Chapter 7 - object description. In Mark S. Nixon and Alberto S. Aguado, editors, *Feature Extraction & Image Processing for Computer Vision (Third Edition)*, pages 343–397. Academic Press, Oxford, third edition edition, 2012.
 13. Christoph Dalitz, Christian Brandt, Steffen Goebbels, and David Kolanus. Fourier descriptors for broken shapes. *EURASIP Journal on Advances in Signal Processing*, 2013(1):1–11, 2013.
 14. Ze Liu, Yutong Lin, Yue Cao, Han Hu, Yixuan Wei, Zheng Zhang, Stephen Lin, and Baining Guo. Swin transformer: Hierarchical vision transformer using shifted windows. In *Proceedings of the IEEE/CVF International Conference on Computer Vision*, pages 10012–10022, 2021.
 15. Yunxiang Li, Guodong Zeng, Yifan Zhang, Jun Wang, Qun Jin, Lingling Sun, Qianni Zhang, Qisi Lian, Guiping Qian, Neng Xia, et al. Agmb-transformer: Anatomy-guided multi-branch transformer network for automated evaluation of root canal therapy. *IEEE Journal of Biomedical and Health Informatics*, 2021.
 16. Yunxiang Li, Shuai Wang, Jun Wang, Guodong Zeng, Wenjun Liu, Qianni Zhang, Qun Jin, and Yaqi Wang. Gt u-net: A u-net like group transformer network for tooth root segmentation. In *International Workshop on Machine Learning in Medical Imaging*, pages 386–395. Springer, 2021.
 17. Zilong Huang, Youcheng Ben, Guozhong Luo, Pei Cheng, Gang Yu, and Bin Fu. Shuffle transformer: Rethinking spatial shuffle for vision transformer. *arXiv preprint arXiv:2106.03650*, 2021.
 18. Prajit Ramachandran, Niki Parmar, Ashish Vaswani, Irwan Bello, Anselm Levskaya, and Jon Shlens. Stand-alone self-attention in vision models. *Advances in Neural Information Processing Systems*, 32, 2019.
 19. Irwan Bello, Barret Zoph, Ashish Vaswani, Jonathon Shlens, and Quoc V. Le. Attention augmented convolutional networks. In *Proceedings of the IEEE/CVF International Conference on Computer Vision (ICCV)*, October 2019.
 20. Ashish Vaswani, Noam Shazeer, Niki Parmar, Jakob Uszkoreit, Llion Jones, Aidan N Gomez, Łukasz Kaiser, and Illia Polosukhin. Attention is all you need. *Advances in neural information processing systems*, 30, 2017.
 21. Simon F Eskildsen, Pierrick Coupé, Vladimir Fonov, José V Manjón, Kelvin K Leung, Nicolas Guizard, Shafik N Wassef, Lasse Riis Østergaard, D Louis Collins, Alzheimer’s Disease Neuroimaging Initiative, et al. Beast: brain extraction based on nonlocal segmentation technique. *NeuroImage*, 59(3):2362–2373, 2012.
 22. Clifford R Jack Jr, Matt A Bernstein, Nick C Fox, Paul Thompson, Gene Alexander, Danielle Harvey, Bret Borowski, Paula J Britson, Jennifer L. Whitwell, Chadwick Ward, et al. The alzheimer’s disease neuroimaging initiative (adni): Mri methods. *Journal of Magnetic Resonance Imaging: An Official Journal of the International Society for Magnetic Resonance in Medicine*, 27(4):685–691, 2008.
 23. Antonios Makropoulos, Emma C Robinson, Andreas Schuh, Robert Wright, Sean Fitzgibbon, Jelena Bozek, Serena J Counsell, Johannes Steinweg, Katy Vecchiato, Jonathan Passerat-Palmbach, et al. The developing human connectome project: A minimal processing pipeline for neonatal cortical surface reconstruction. *Neuroimage*, 173:88–112, 2018.
 24. Jun-Yan Zhu, Taesung Park, Phillip Isola, and Alexei A Efros. Unpaired image-to-image translation using cycle-consistent adversarial networks. In *Proceedings of the IEEE international conference on computer vision*, pages 2223–2232, 2017.

25. Yue Sun, Kun Gao, Zhengwang Wu, Guannan Li, Xiaopeng Zong, Zhihao Lei, Ying Wei, Jun Ma, Xiaoping Yang, Xue Feng, et al. Multi-site infant brain segmentation algorithms: The iseg-2019 challenge. *IEEE Transactions on Medical Imaging*, 40(5):1363–1376, 2021.
26. Dequan Wang, Evan Shelhamer, Shaoteng Liu, Bruno Olshausen, and Trevor Darrell. Tent: Fully test-time adaptation by entropy minimization. In *International Conference on Learning Representations*, 2021.